

Modified nano-crystalline ferrites for high-temperature WGS membrane reactor applications

Ataullah Khan^a, Ping Chen^b, P. Boolchand^b, Panagiotis G. Smirniotis^{a,*}

^a Department of Chemical and Materials Engineering, University of Cincinnati, USA

^b Department of Electrical and Computer Engineering and Computer Science, University of Cincinnati, USA

Received 9 July 2007; revised 6 October 2007; accepted 21 October 2007

Available online 26 November 2007

Abstract

In the present study, selected metal ions ($M = \text{Cr, Mn, Co, Ni, Cu, Zn, and Ce}$) were introduced into iron oxide (spinel lattice) and screened for effectiveness for a high-temperature water–gas shift reaction. Simultaneous precipitation of Fe(III) nitrates along with metal nitrate(s) at optimal concentrations resulted in the formation of high-surface area nanosized catalysts. A noticeable interaction between iron and the other substituent metal was interpreted from the formation of either inverse or mixed spinels of composition $A_{(1-\delta)}B_{\delta}[A_{\delta}B_{(2-\delta)}]O_4$. The incorporation of metal cations into the hematite crystal structure modified the magnetic hyperfine field and also influenced the reducibility of hematite particles, as observed in Mössbauer effect and temperature-programmed reduction studies. These effects strongly depend on the nature of incorporated metal cations. Mössbauer hyperfine fields, isomer shifts and transmission electron microscopy findings support nanoscale nature of the catalysts. Amongst catalysts tested, Fe/Cr and Fe/Ce are found to be the most active, with activity approaching equilibrium conversion at high temperatures. © 2007 Elsevier Inc. All rights reserved.

Keywords: HT WGS; Nanosized; Modified ferrites; Mössbauer; TPR

1. Introduction

The water–gas shift (WGS) reaction using membrane reactors are attractive largely because hydrogen can be selectively permeated through a membrane, making complete conversion possible [1,2]. In this manner, the broad consequences of complete conversion can be explored. The underlying issues have been examined by several authors through feasibility studies and computational and real-time analyses [1–6]. A membrane reactor typically operates at high temperatures and high pressures [7]. Among the various membrane tested, silica-based membranes have been found to be thermally robust, permeable, and permselective for H_2 over other gases in the syngas reactant mixture [8–10].

Substitution of ‘Fe’ cation sites by other metal (M) atom substituents in the ferrite structure generally promotes formation of mixed ($0 < \delta < 1$) or inverse ($\delta = 1$) spinel $A_{(1-\delta)}B_{\delta}$ -

$[A_{\delta}B_{(2-\delta)}]O_4$ structures, where δ is the degree of inversion [11,12]. For a normal spinel, AB_2O_4 , $\delta = 0$, whereas for an inverse spinel, $B[AB]O_4$, $\delta = 1$. The physicochemical properties of ferrites are strongly dependent on the site, nature, and amount of M substituents at the A and B sites in the structure. Furthermore, ion sizes also can significantly influence the covalency effect (2^+ to 3^+ exchange), which is of much interest in the present work. In most instances, these substitutions improve thermal and textural stability while promoting reducibility ($Fe_2O_3 \rightarrow Fe_3O_4$) [13,14]. Transition and inner transition metal substituents can be expected to strongly modify the redox properties, that is, the $Fe^{3+} \leftrightarrow Fe^{2+}$ charge transfer rate.

The present investigation was aimed at developing new high-temperature catalysts for the WGS reaction that can operate in extreme conditions as posed in the membrane reactor regime. In this work, metal (M)-doped ferrite catalysts using either the first-row transition atoms ($M = \text{Cr, Mn, Co, Ni, Cu}$), the nontransition atom ($M = \text{Zn}$), or the inner-transition atom ($M = \text{Ce}$) series were considered. These catalysts were synthe-

* Corresponding author. Fax: +1 513 556 3473.

E-mail address: panagiotis.smirniotis@uc.edu (P.G. Smirniotis).

sized and their performance for the WGS reaction evaluated. Metal dopant additives (M) influence the physicochemical, the structural properties and catalytic performance. The experiments were performed in a temperature range of 350–550 °C. A relatively high space velocity of 60,000 h⁻¹ was maintained in the WGS reactor. Different ratios of steam/CO (1, 3.5, and 7) were used to investigate the performance of the catalysts in the WGS reaction. The shift activity was found to increase with increasing temperature and also with increasing steam/CO ratios. Interestingly, at high temperatures, the activity approached the equilibrium conversion value over Fe/Cr and Fe/Ce catalysts. Among the various catalysts studied, Fe/Ce is found to be an ideal catalyst for operating in steam-rich conditions. The information obtained from various techniques, including X-ray diffraction (XRD), temperature-programmed reduction (TPR), pore size distribution (PSD), Mössbauer spectroscopy, and transmission electron microscopy (TEM), is used to fully characterize the crystalline structure and morphology of the catalysts and their WGS activity. The findings indicate that WGS activity is determined by the operating conditions used in a given case.

2. Experimental

2.1. Catalyst preparation

Selected metal-doped iron oxide-based catalysts with nominal composition of Fe_{1.82}M_{0.18}O₃ (where M = Cr, Mn, Co, Ni, Cu, Zn, and Ce) were prepared in 10:1 (Fe:M) atomic ratio by the co-precipitation route. Nitrate precursors were used for all of the preparations. In a typical preparation, calculated amounts of iron nitrates and the corresponding dopant metal nitrate were dissolved separately in deionized water and mixed together. Dilute aqueous ammonia was gradually added dropwise to the aforementioned mixture solutions under vigorous stirring until precipitation was complete (pH 8.5). The supernatant liquid was analyzed for nitrate ions by adding about 1 mL of concentrated sulfuric acid to 10 mL of the supernatant; the formation of [Fe(NO)]²⁺ is indicated by a brown ring [15]. No brown ring formation was observed in any case. The precipitate gels thus obtained were further aged overnight and filtered off. The resulting cakes were oven-dried at 80 °C for 12 h and finally calcined at 500 °C for 3 h in an inert environment. The heating and cooling rates were maintained at 5 °C/min.

The precipitation process is dictated by solution thermodynamics. The solution reaches saturation state when the dissolution rate equals the precipitation rate, and nucleation starts when the solution concentration exceeds the saturation concentration. The solution concentration affects the crystallite size of the precipitated catalyst. In the present investigation, the concentration of the nitrate solution was optimized so as yield nanosized grains [16]. It is notable that all catalysts reported herein were prepared by analogous procedures, which was necessary to allow direct comparison of their catalytic properties.

2.2. Catalyst characterization

2.2.1. Surface area and pore size distribution analysis

The BET surface areas were obtained by N₂ adsorption on a Micromeritics Gemini 2360 instrument. Before analysis, the samples were oven-dried at 120 °C for 12 h and flushed with argon for 2 h. The pore size distribution analyses were conducted by N₂ physisorption at liquid N₂ temperature using a Micromeritics ASAP 2010 apparatus. All samples were degassed at 300 °C under vacuum before analysis.

2.2.2. XRD measurements

Powder XRD patterns were recorded on a Phillips X'pert diffractometer using nickel-filtered CuK α (0.154056 nm) as the radiation source. The intensity data were collected over a 2 θ range of 3–80° with a step size of 0.02° using a counting time of 1 s per point. Crystalline phases were identified through comparison with the reference data from ICDD files. Lattice parameter estimations were done by standard indexing methods, using the intensity of high 2 θ peaks (214) and (300) [17–19].

2.2.3. TPR measurements

Hydrogen TPR of various catalyst samples was performed using an automated catalyst characterization system (Micromeritics model AutoChem II 2920) with a thermal conductivity detector (TCD), at a heating rate of 5 °C/min. The reactive gas composition was H₂ (10 vol%) in argon, and the flow rate was fixed at 10 mL/min (STP). The total reactive gas consumption during TPR analysis was measured. The TPR measurements were done after activation once the sample was cooled to 50 °C in a helium flow. The sample was then held at 50 °C under flowing helium to remove the remaining adsorbed oxygen until the TCD signal returned to the baseline. Subsequently, the TPR experiments were performed up to 800 °C.

2.2.4. Mössbauer spectral analysis

⁵⁷Fe Mössbauer spectra were recorded in transmission geometry using a constant acceleration spectrometer with a liquid He metal dewar. Experiments were performed either at room temperature or at –195 °C. A 20 mCi sample of ⁵⁷Co (Rh) was used as an emitter, and the spectrometer was calibrated using a α -Fe foil and taking the isomer shift of Rh at –0.116 mm/s with respect to α -Fe. Line widths on the inner two lines of α -Fe were typically 0.21 mm/s. An 80-mg quantity of the oxide catalyst in fine powder form was spread onto a thin Teflon sheet using GE varnish as a binder for use as an absorber. A typical run lasted 24 h, and base line counts were 2 million per channel. Samples that did not reveal a magnetic Zeeman splitting at 27 °C were examined further at –195 °C.

2.2.5. TEM

TEM was performed with a Philips CM 20 electron microscope. The accelerating voltage was 200 keV, with an LaB₆ emission current and a point-to-point resolution of 0.27 nm. Samples were sonically dispersed in ethanol and deposited on a holey carbon Cu grid before examination. Once the solvent was

evaporated, the particles remaining on the borders of the holes in the carbon film were studied.

2.3. Catalyst activity

The WGS reaction was carried out in a vertical downflow fixed-bed differential ceramic microreactor (0.635 cm i.d.) at atmospheric pressure. In a typical experiment, ca. 0.1 g of sieved catalyst was placed between two quartz wool plugs. The reactor was placed vertically inside a programmable tubular furnace (Lindberg), which was heated electrically. Before the reaction, the catalyst was pretreated in flowing process gas at 400 °C for 4 h. The catalyst pretreatment involved the partial reduction of hematite (Fe_2O_3) to magnetite (Fe_3O_4) using a mixture of H_2 , CO , CO_2 (99.9% pure gases), and water vapor [20–22], taking care to avoid overreduction of the magnetite active phase to lower carbides, oxides, or metallic iron phases. (Metallic iron phases are active catalysts for methanation and Fischer–Tropsch processes [20].) The heating and cooling rate was maintained at 5 °C/min. The gas flows were regulated through precalibrated mass flow controllers with a digital read-out unit (MKS Instruments). Water was injected into the system through a motorized syringe pump (Cole-Parmer type 74900) to generate steam. The entire system was maintained at 200 °C using heating tapes. Before pretreatment, the reactor setup was flushed with an inert gas. The pretreatment gas mixture was initialized only after the catalytic system had reached ≥ 150 °C.

The experiments were performed at 350–550 °C using a designated amount of steam and CO . The product stream coming from the reactor was passed through ice cooled trap to condense water, after which, the product gases were analyzed with an on-line TCD (Gow Mac series 550) with a Porapak Q column to separate the gases. The TCD was interfaced to a personal computer using a peak simple chromatography data system. The results were analyzed using the Peak Simple 2.31 program. The product gas was injected through a six-port valve, with sampling performed at 20-min intervals. Reported values of conversions correspond to steady-state values (0.5 h). A gas hourly space velocity of $60,000 \text{ h}^{-1}$ was maintained throughout the experiments. To investigate the influence of the steam/dry gas ratio on the progress of the WGS reaction, different steam/dry gas ratios (1, 3.5, and 7) were used.

3. Results and discussion

3.1. BET surface area and pore size distribution measurements

Table 1 gives various physical properties (BET surface area, average pore size, crystallite size and lattice variables) of the metal-doped iron oxide-based catalysts $\text{Fe}_{1.82}\text{M}_{0.18}\text{O}_3$ ($\text{M} = \text{Cr, Mn, Co, Ni, Cu, Zn, and Ce}$) prepared in this work. It is evident from the table that all of the iron oxide-based catalysts prepared in the present investigation exhibited remarkably high surface areas. The surface area measurements clearly reveal that the surface area of iron-based mixed oxides can be altered by

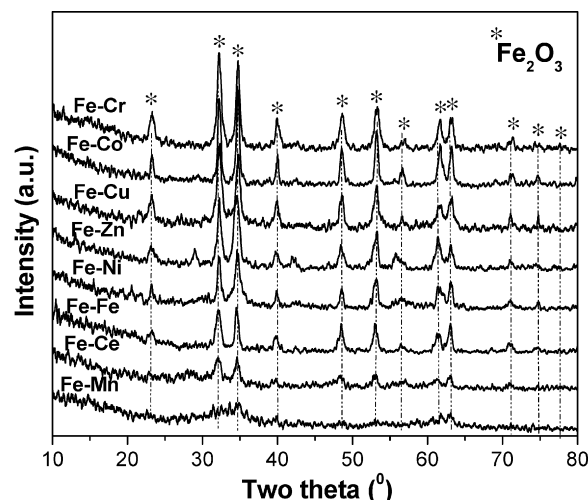


Fig. 1. X-ray powder diffraction patterns of various $\text{Fe}_{1.82}\text{M}_{0.18}\text{O}_3$ ($\text{M} = \text{Cr, Mn, Co, Ni, Cu, Zn, and Ce}$) catalysts.

the addition of different transition/inner-transition metals. The efficacy of the (dopant ions) foreign cations in modifying the resultant specific surface area can be directly related to variations in the rate of crystal growth. The nature and concentration of the foreign cations present in the system govern this variation. Interestingly, a narrow pore size distribution (mesoporous regime) was observed in all of the investigated catalyst systems in the range of 49–250 Å (Table 1).

3.2. XRD studies

To ascertain the composition and phase purity, the catalysts were examined by XRD. The powder XRD patterns of various $\text{Fe}_{1.82}\text{M}_{0.18}\text{O}_3$ ($\text{M} = \text{Cr, Mn, Fe, Co, Ni, Cu, Zn, and Ce}$) catalysts investigated in the present study are shown in Fig. 1. Interestingly, all of the modified ferrite samples (except Fe/Mn and Fe/Ce) exhibit intense and similar XRD patterns, with well-resolved peaks clearly indicating the polycrystalline and monophasic nature of the samples. The existence of a Fe_2O_3 -type phase (PDF-ICDD 33-0664) was identified by comparing the patterns with standard reference data from the PDF database. The observation of a hematite phase in all of the catalysts is of significance, because during catalyst activation, the hematite phase is converted to the magnetite phase (Fe_3O_4), the active phase for the WGS reaction. In addition, the XRD spectra for the modified ferrite samples show no extra crystalline phases due to individual oxides of the substituent cations, such as MO_x ($\text{M} = \text{Cr, Mn, Co, Ni, Cu, Zn, and Ce}$). Any WGS catalyst based on iron, has to undergo the required transformation (reduction) from hematite to magnetite, where the active catalyst comprises a crystalline inverse spinel structure in which the octahedral lattice sites are occupied equally by Fe^{2+} and Fe^{3+} ions. The X-ray diffraction experiments performed on activated catalysts, confirmed the existence of Fe_3O_4 phase (PDF-ICDD 26-1136) (supporting information). Magnetite (Fe_3O_4) crystallizes in a cubic inverse spinel structure (AB_2O_4 type) at RT, where 1/3 of the Fe ions occupies tetrahedrally coordinated A sites as Fe^{3+} and remaining 2/3 of the Fe ions with equal num-

Table 1
BET surface area, XRD phase, cell parameter, and cell volume measurements

Metal doped iron oxide based catalysts $\text{Fe}_{2-x}\text{M}_x\text{O}_3$	Physisorption measurements		XRD phase ^a	XRD analyses			TEM grain size (nm)
	BET SA (m^2/g)	Average pore diameter (\AA)		Cell parameter		Cell volume (\AA^3) ^b	
				a (\AA) ^b	c (\AA) ^b	Axial ratio c/a	
$\text{Fe}_{1.82}\text{Cr}_{0.18}\text{O}_3$	81.7	77	Fe_2O_3	5.094	13.834	2.716	310.9
$\text{Fe}_{1.82}\text{Mn}_{0.18}\text{O}_3$	175.9	119	Fe_2O_3	nd ^c	nd	nd	nd
Fe_2O_3	36.3	250	Fe_2O_3	5.093	13.912	2.731	316.0
$\text{Fe}_{1.82}\text{Co}_{0.18}\text{O}_3$	41.0	104	Fe_2O_3	5.091	13.858	2.722	311.1
$\text{Fe}_{1.82}\text{Ni}_{0.18}\text{O}_3$	80.1	49	Fe_2O_3	5.097	14.097	2.765	317.2
$\text{Fe}_{1.82}\text{Cu}_{0.18}\text{O}_3$	75.3	120	Fe_2O_3	5.106	14.109	2.763	318.9
$\text{Fe}_{1.82}\text{Zn}_{0.18}\text{O}_3$	46.1	116	Fe_2O_3	5.114	14.117	2.760	319.7
$\text{Fe}_{1.82}\text{Ce}_{0.18}\text{O}_3$	95.9	77	Fe_2O_3	nd	nd	nd	nd

^a Fe_2O_3 (hematite) PDF-ICDD 33-0664.

^b Calculated following standard indexing procedures (Refs. [17–19]).

^c nd: not determined.

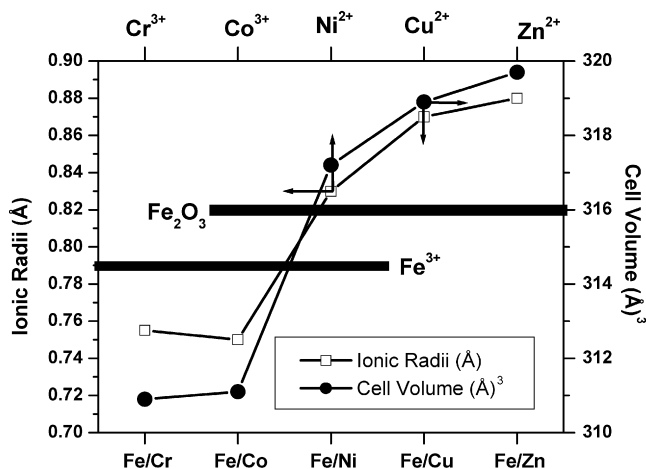


Fig. 2. Relationship between cell volume and ionic radii of substituent ions in various $\text{Fe}_{1.82}\text{M}_{0.18}\text{O}_3$ ($\text{M} = \text{Cr}, \text{Co}, \text{Ni}, \text{Cu}, \text{and Zn}$) catalysts.

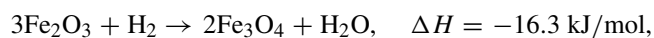
bers of Fe^{2+} and Fe^{3+} are located on octahedrally coordinated B sites. It is well established fact that rapid electron hopping between $\text{Fe}^{2+} \rightleftharpoons \text{Fe}^{3+}$ in the Fe_3O_4 lattice system is needed for carrying out the water gas shift reaction [23]. There was no evidence of the formation of Fe (metallic) or Fe_2C (iron carbide) phases due to possible over-reduction in the present investigation.

Using the interplanar spacing values, calculation of the cell parameters was carried out (Table 1), which revealed that all the substituent ions enter the hematite lattice under the preparation conditions employed in this work. The relationship between the ionic radii of substituent ion and the resultant cell volume is presented in Fig. 2. The substitution of Fe^{3+} ($r = 0.785 \text{ \AA}$) with M^{n+} ($\text{M} = \text{Cr}, \text{Mn}, \text{Co}, \text{Ni}, \text{Cu}, \text{Zn}, \text{and Ce}$) leads to a modification of the distances between atomic planes, as well as of the lattice constant as shown in Fig. 2 and Table 1. Experimental values of lattice constant were calculated from higher 2θ lines i.e., from (214) and (300) planes for each sample [19]. By comparing the values of the modified ferrite samples with that of the pure Fe_2O_3 sample, prepared by an identical method, it is observed that the lattice expansion is taking place, except in the case of Fe/Cr and Fe/Co systems. All the foreign cations [ionic radii (r_{ion}) $\text{Ni}^{2+} 0.83 \text{ \AA}$; $\text{Cu}^{2+} 0.87 \text{ \AA}$; $\text{Zn}^{2+} 0.88 \text{ \AA}$] except

Cr^{3+} and Co^{3+} ($\text{Cr}^{3+} 0.755 \text{ \AA}$; $\text{Co}^{3+} 0.75 \text{ \AA}$) possess larger ionic radii than Fe^{3+} thereby lead to lattice (cell volume) expansion. On the contrary, when Cr^{3+} and Co^{3+} replace Fe^{3+} ions from their octahedral positions, the distance between is reduced thereby causing lattice (cell volume) contraction. Magnetite is a spinel and possess both tetrahedral and octahedral iron sites. Hematite, on the other hand possesses only octahedral iron sites. With trivalent iron there are five 'd' electrons in the '3d' orbitals. In the high spin state, each of these would be unpaired and occupy all of the t_{2g} and e_g orbitals in an octahedrally coordinated environment or all of the t_2 and e sites in a tetrahedrally coordinated environment. Since there are no degeneracies, the C.F.S.E. for each of these coordinations is zero. Thus there is no preference for either coordination. The alteration in the lattice parameter upon M^{n+} (substituent cation) substitution suggests the incorporation of M^{n+} into the spinel structure.

3.3. Catalyst activation

The fresh catalysts in the hematite form ($\alpha\text{-Fe}_2\text{O}_3$), have to be transformed into magnetite form (Fe_3O_4). This is achieved by controlled reduction of $\alpha\text{-Fe}_2\text{O}_3$ into Fe_3O_4 in a flow of process gas mixture ($\text{CO}, \text{CO}_2, \text{H}_2$, and steam- H_2O). The representative reactions are shown as follows:



The reduction is typically performed during the HTS reactor startup, and it should be carefully controlled because of a significant heat release resulting from the exothermic nature of the reactions involved, which may damage the catalyst [24]. The over-reduction should be avoided, as it leads to the formation of FeO, Fe_2C and metallic iron phases, which catalyze undesired side reactions (i.e., methanation and CO disproportionation). The ratio of oxidant to reductant (also called "reduction factor," R) in the process gas mixture has to be just optimal, in order to facilitate the reduction of hematitic to magnetitic phase and should not catalyze further reduction. In the present study $R = 1.4$ was utilized; where $R = [(\text{CO}) + (\text{H}_2)]/[(\text{CO}_2) + (\text{H}_2\text{O})]$.

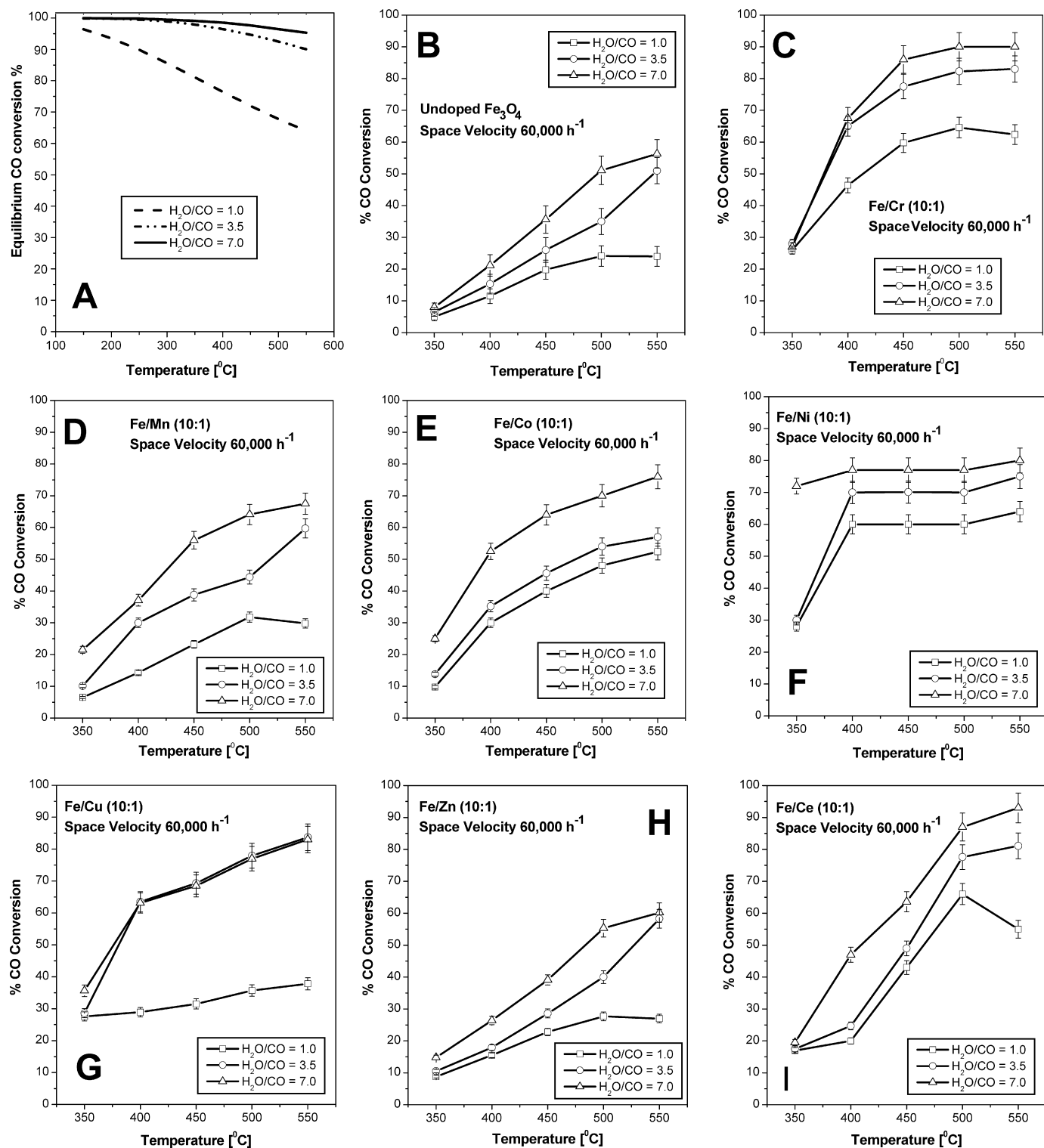


Fig. 3. The WGS activity results of various $\text{Fe}_{2.73}\text{M}_{0.273}\text{O}_4$ ($\text{M} = \text{Cr, Mn, Co, Ni, Cu, Zn, and Ce}$) activated catalysts in the temperature range 350–550 °C; steam/CO = 1, 3.5, and 7.0; gas hourly space velocity (GHSV) = 60,000 h^{-1} ; (A) shows the variation of the thermodynamic equilibrium conversion of CO (%) as a function of steam-to-CO (S/CO) ratio in the feed at different temperatures; (B) represents WGS activity over pure Fe_3O_4 (undoped) sample.

3.4. WGS activity

The WGS reaction is a moderately exothermic reaction. As shown in Fig. 3A, the equilibrium conversion of CO decreases as the reaction temperature increases and increases with

increase in steam-to-CO ($\text{H}_2\text{O}/\text{CO}$) ratio. No pressure drop across the catalyst bed was observed during the experiments nor was CH_4 formed in the effluent stream (except in the case of Fe/Mn). The results of the experiments carried out at different temperatures and different $\text{H}_2\text{O}/\text{CO}$ ratios, over various

modified ferrite-based shift are shown in Figs. 3C–3I. For the sake of better comparison WGS activity results over undoped Fe_3O_4 activated catalyst are presented in Fig. 3B. The activity increased with the temperature, due to kinetic factors [25] and this also shows that the catalysts are stable in these conditions. It is well known that under low steam to CO ratio or high temperatures metallic iron or a carbide phase may be formed. These phases can act as Fischer–Tropsch (FT) catalysts. However, except for the presence of Fe_3O_4 phase, no other XRD phases could be detected in the present study (except in the case of Fe/Mn). The lower WGS activity observed at 350 °C, can be related to the difficulty in sustaining the active magnetite phase, as observed from TPR experiments (presented later). It is also suggested that at lower temperatures the activity of magnetite is limited by the dissociation of steam [26]. The WGS reaction was performed at different steam-to-CO ratios ($S/\text{CO} = 1, 3.5,$ and 7.0) to mimic steam deficient to steam rich conditions respectively, and to study the influence of steam on the eventual activity performance of our catalysts. A relatively high space velocity of $60,000 \text{ h}^{-1}$ was maintained in all of the experiments. The WGS reaction was performed in the temperature range of 350–550 °C. In general, WGS activity increased with increasing temperature. In addition, the WGS activity increased with increasing steam-to-CO ratio. The activity approached the equilibrium conversion at higher temperatures over Fe/Cr and Fe/Ce catalysts. On the whole, it is observed that, among the various modified ferrites investigated in this study, Fe/Ce is a promising system for performing the WGS reaction under steam-rich and high-temperature conditions. In a membrane reactor operation, the catalyst is exposed to a steam-rich environment and high temperatures (severe operation conditions). All of the present results were successfully reproduced twice within the limits of permissible error.

3.5. TPR

Iron can exist in the form of three oxides: hematite (Fe_2O_3), magnetite (Fe_3O_4), and wustite (FeO). The latter is unstable below 570 °C, where it decomposes to $\alpha\text{-Fe}$ and Fe_3O_4 . At temperatures below 570 °C, the reduction of Fe_2O_3 to Fe metal proceeds in two steps via an Fe_3O_4 intermediate [27]. $\text{Fe}_2\text{O}_3 \rightarrow \text{Fe}_3\text{O}_4$ reduction is exothermic, whereas reduction to the metal is endothermic [28]. In reduction of either hematite or magnetite at temperatures above 600 °C, the formation of a stable wustite phase also must be considered. In TPR of pure hematite (Fe_2O_3), the first reduction peak appeared at 302 °C, corresponding to the transition of Fe_2O_3 to Fe_3O_4 . The second peak at 354 °C was attributed to the transformation of Fe_3O_4 to FeO . The third and final peak at 475 °C corresponds to the transition of FeO to Fe [29]. In another report, the TPR curves of hematite exhibited a peak at 510 °C, attributed to magnetite formation, and another peak at around 770 °C, attributed to the formation of metallic iron [30]. The position of the temperature maxima may vary from sample to sample depending on the particle size and other parameters, such as temperature ramp rate. The addition of a substituent/dopant ion significantly modifies

the reduction profile compared with that of the pristine Fe_2O_3 sample [31].

The TPR profiles of the various metal-doped iron oxide-based catalysts are presented in Figs. 4a and 4b, and the corresponding T_{max} values for each reduction step of iron oxide are given in Table 2. The TPR experiments were repeated three times on all of these samples to check for reproducibility; similar line shapes were observed for all of the catalyst samples. For reference purposes, the TPR profile of pristine Fe_2O_3 (free from any substituent ion) prepared by a similar procedure is shown in Fig. 4A. In the TPR of pristine hematite (Fe_2O_3), the first reduction peak appeared at 348 °C, corresponding to the reductive transition of Fe_2O_3 to Fe_3O_4 . The peak at 621 °C corresponds to the transformation of Fe_3O_4 to FeO . Within the experimental conditions of the present study, formation of metallic iron species was either delayed (prolonged) or not observed, which can be attributed to the preparation method used in this investigation.

From Figs. 4B–4H and Table 2, it is obvious that each promoter ($M = \text{Cr}, \text{Mn}, \text{Co}, \text{Ni}, \text{Cu}, \text{Zn},$ and Ce) influenced the reduction profile of iron oxide in a unique manner. In the case of Fe/Cr catalyst, the first reduction peak at 225 °C corresponded to the reduction of $\text{Cr}^{6+} \rightarrow \text{Cr}^{3+}$ (Fig. 4B); interestingly, further partial reduction of $\text{Cr}^{3+} \rightarrow \text{Cr}^{2+}$, which would be expected at 490 °C [32], was not observed. Reduction of $\text{Fe}_2\text{O}_3 \rightarrow \text{Fe}_3\text{O}_4$ was observed at $T_{\text{max}} 350$ °C, whereas further reduction to FeO occurred at higher temperatures. Adding chromium to Fe_2O_3 did not improve the reducibility of hematite to magnetite. In the Fe/Mn catalyst, the first reduction peak at 200 °C corresponded to the reduction of $\text{Mn}^{4+} \rightarrow \text{Mn}^{3+}$, whereas the reduction of $\text{Mn}^{3+} \rightarrow \text{Mn}^{2+}$ occurred at 528 °C (Fig. 4C). In particular, the Fe/Mn system presents a typical example of the cooperative synergistic influence of Mn and Fe on each other's reduction profile. An important feature observed in the TPR profile of Fe/Mn is a shift of the iron oxide TPR peaks to lower temperatures (by ~ 50 °C) as manganese is introduced into the hematite host lattice. Thus, this shift indicates that the presence of Mn facilitates the reduction of Fe^{3+} species (Fe_2O_3 to Fe_3O_4). The 613 °C T_{max} peak corresponds to the reduction of magnetite to wustite, beyond which total reduction to metallic iron would be expected. The reduction profile for pristine Co_3O_4 comprises a low-temperature peak below ~ 300 °C [33] or ~ 330 °C [34] and a high-temperature peak between 350 and 600 °C [34] or, as reported by Brown et al. [33], between 300 and 700 °C, corresponding to the following reductive processes: $\text{Co}_3\text{O}_4 \rightarrow \text{CoO} \rightarrow \text{Co}$. The addition of cobalt to iron oxide lowered the temperature of the maximum rate of hydrogen uptake [for $\text{Fe}_2\text{O}_3 \rightarrow \text{Fe}_3\text{O}_4$] by 20 °C (from 350 to 330 °C), demonstrating that the presence of cobalt makes the hematite easier to reduce (Fig. 4D). The observed TPR pattern matches well with the literature reports on iron-cobalt catalysts [33]. In the TPR profile of Fe/Ni (Fig. 4E), the reduction of hematite to magnetite occurred at 327 °C, followed by the reduction of Ni^{2+} to Ni^0 at ~ 510 °C. Finally, the reductive transition of magnetite to wustite occurred at 590 °C. The formation of metallic iron could not be observed even up to 800 °C. In the Fe/Cu catalyst (Fig. 4F), the first peak at 143 °C corresponds to the reduction

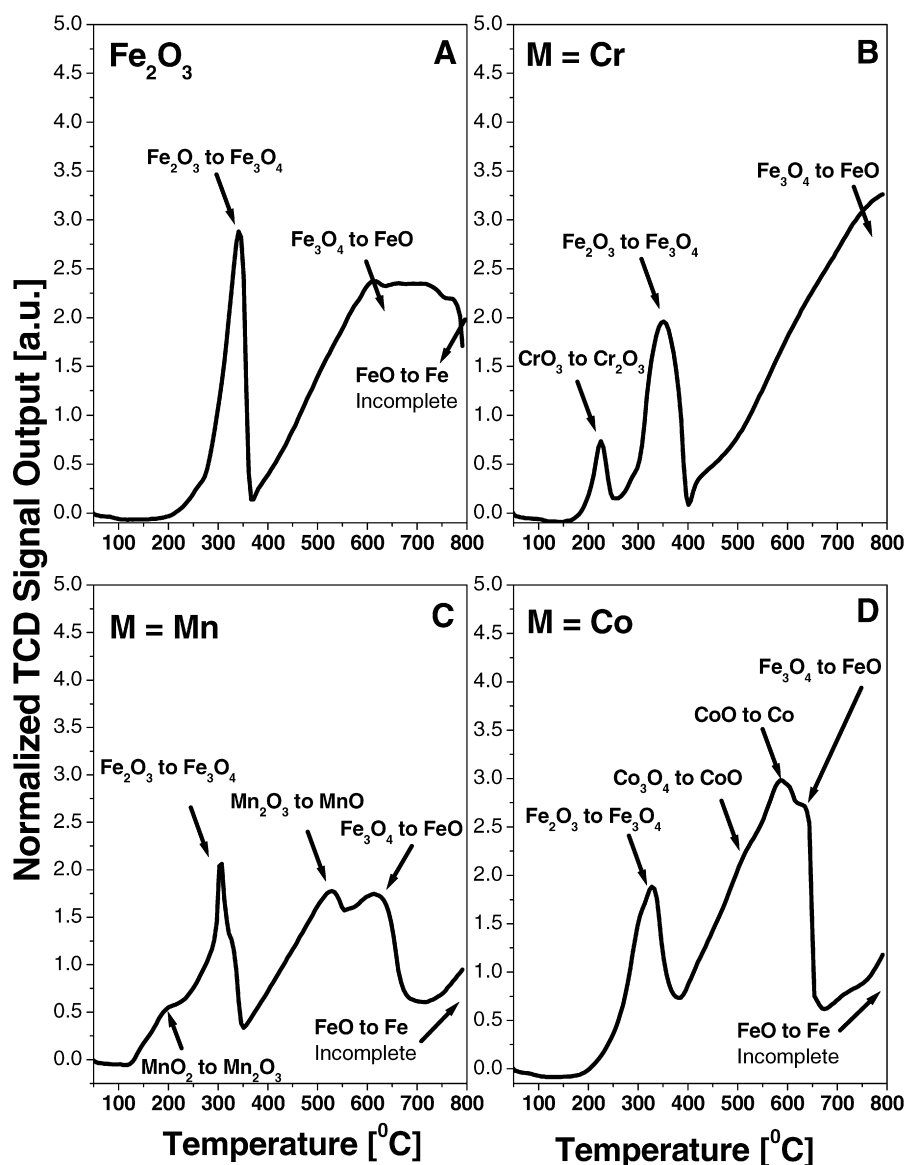


Fig. 4. (a) TPR profiles of titled $\text{Fe}_{1.82}\text{M}_{0.18}\text{O}_3$ ($\text{M} = \text{Cr}, \text{Mn}, \text{and Co}$) catalysts.

of $\text{Cu}^{2+} \rightarrow \text{Cu}^+$ and the subsequent peak at 162°C corresponds to the reduction of $\text{Cu}^+ \rightarrow \text{Cu}^0$ [35,36]. An interesting observation from the present study is that the addition of Cu to Fe_2O_3 , decreased the reduction temperature of hematite to magnetite considerably, to 190°C , compared with 348°C for the pristine hematite sample. Interestingly, the incorporation of Cu did not affect the stability of the Fe_3O_4 phase, which was found to be stable up to 600°C , after which transformation of the magnetite to wustite was observed. The TPR profile of the Fe/Zn catalyst (Fig. 4G) was very similar to that of the pristine- Fe_2O_3 sample. The peak at 333°C can be attributed to the formation of magnetite phase, whereas reduction of Zn^{2+} to Zn^0 was observed at about 588°C , beyond which formation of wustite phase was noted. The enhanced reducibility observed in the Fe/Ce catalyst (Fig. 4H) may be related to the close interaction between Fe and Ce cations occurring during the co-precipitation process. Pristine CeO_2 exhibited two characteristic reduction regimes: surface shell reduction (485°C) and bulk reduction (850°C)

[34]. Promoting iron oxide with cerium causes a shift in the reduction peaks of both hematite-to-magnetite and magnetite-to-wustite to lower temperatures (Table 2). In the Fe/Ce system, the ceria surface shell reduction occurs at 380°C , instead of 485°C as in the pristine ceria sample; however, the ceria bulk reduction was not affected by the presence of iron [34]. According to Giordano et al. [37], the TPR profile for ceria is not controlled by the rate of diffusion of the oxygen vacancies; instead, surface reduction process and the difference of both thermodynamic and kinetic properties in the ceria microcrystals (as a function of their size) are critical factors. The WGS reaction is a redox process wherein facile reducibility of Fe^{3+} species enhances the WGS activity.

3.6. Mössbauer spectroscopy studies

^{57}Fe Mössbauer spectroscopy provides an elegant local probe of Fe cations in metal-doped ferrites. These results are

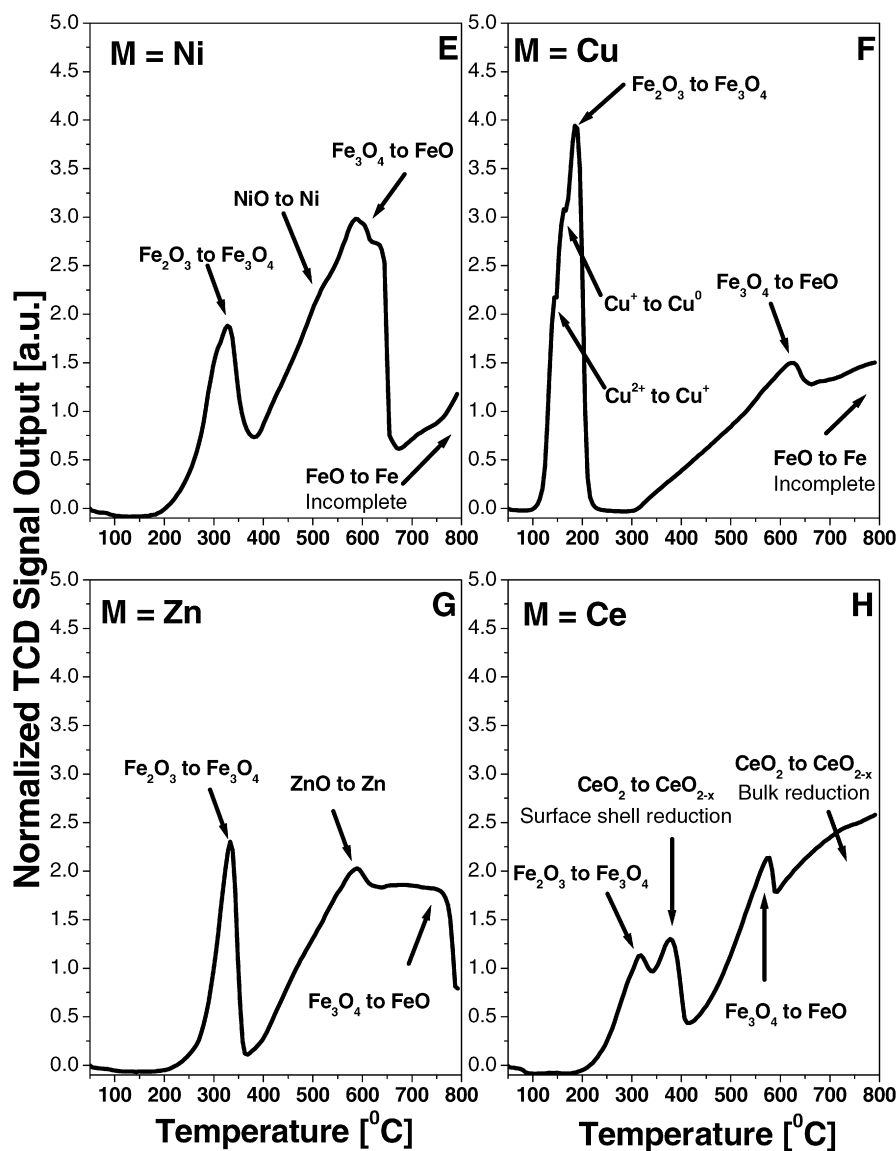


Fig. 4. (b) TPR profiles of titled $\text{Fe}_{1.82}\text{M}_{0.18}\text{O}_3$ ($\text{M} = \text{Ni}, \text{Cu}, \text{Zn}, \text{and Ce}$) catalysts.

Table 2
 T_{max} ($^{\circ}\text{C}$) values pertaining to each reduction step of iron oxide

Metal-promoted $\text{Fe}_{2-x}\text{M}_x\text{O}_3$ catalysts	T_{max} ($^{\circ}\text{C}$)		
	$\text{Fe}_2\text{O}_3 \rightarrow \text{Fe}_3\text{O}_4$	$\text{Fe}_3\text{O}_4 \rightarrow \text{FeO}$	$\text{FeO} \rightarrow \text{Fe}$
$\text{Fe}_{1.82}\text{Cr}_{0.18}\text{O}_3$	350	~800	>800
$\text{Fe}_{1.82}\text{Mn}_{0.18}\text{O}_3$	300	613	>800
Fe_2O_3	348	621	>800
$\text{Fe}_{1.82}\text{Co}_{0.18}\text{O}_3$	330	623	>800
$\text{Fe}_{1.82}\text{Ni}_{0.18}\text{O}_3$	327	590	>800
$\text{Fe}_{1.82}\text{Cu}_{0.18}\text{O}_3$	190	650	>800
$\text{Fe}_{1.82}\text{Zn}_{0.18}\text{O}_3$	333	~700	>800
$\text{Fe}_{1.82}\text{Ce}_{0.18}\text{O}_3$	319	578	>800
$\text{Fe}_2\text{O}_3^{\text{a}}$	302	354	475
$\text{Fe}_2\text{O}_3^{\text{b}}$	510	–	770

^a Ref. [29].

^b Ref. [30].

important, because small variations in the substitution of Fe(II) or Fe(III) leads to major changes in the chemical properties and functionality of these materials. Some parameters, such as

the crystal field stabilization energy (CFSE) of metallic ions with different electronic configurations, polarization, and repulsion effects, apparently affect the total energy and preferred symmetry of the resulting compounds. Thus, doping effects can lead to the crystallization of an ideal inverse spinel or a normal or mixed spinel structure. Substitution of iron sites with other substituent cations apparently modifies the redox ability of ferrites, and also influences their chemical stability. In magnetite-type structures, octahedral sites are occupied by 2^+ and 3^+ ions, whereas tetrahedral sites are occupied by 3^+ ions only. Reithwisch and Dumesic [38] studied a number of spinel-based materials and concluded that only inverse and mixed spinel structures readily undergo rapid electron exchange between the 2^+ and 3^+ states, thereby catalyzing the WGS reaction [38]. The significance of the $2^+ \rightleftharpoons 3^+$ redox couple also was demonstrated by Boreskov [39]. Encouraging tetrahedral sites to expand and octahedral sites to contract results in improved covalency of the system and promotes electron-hopping

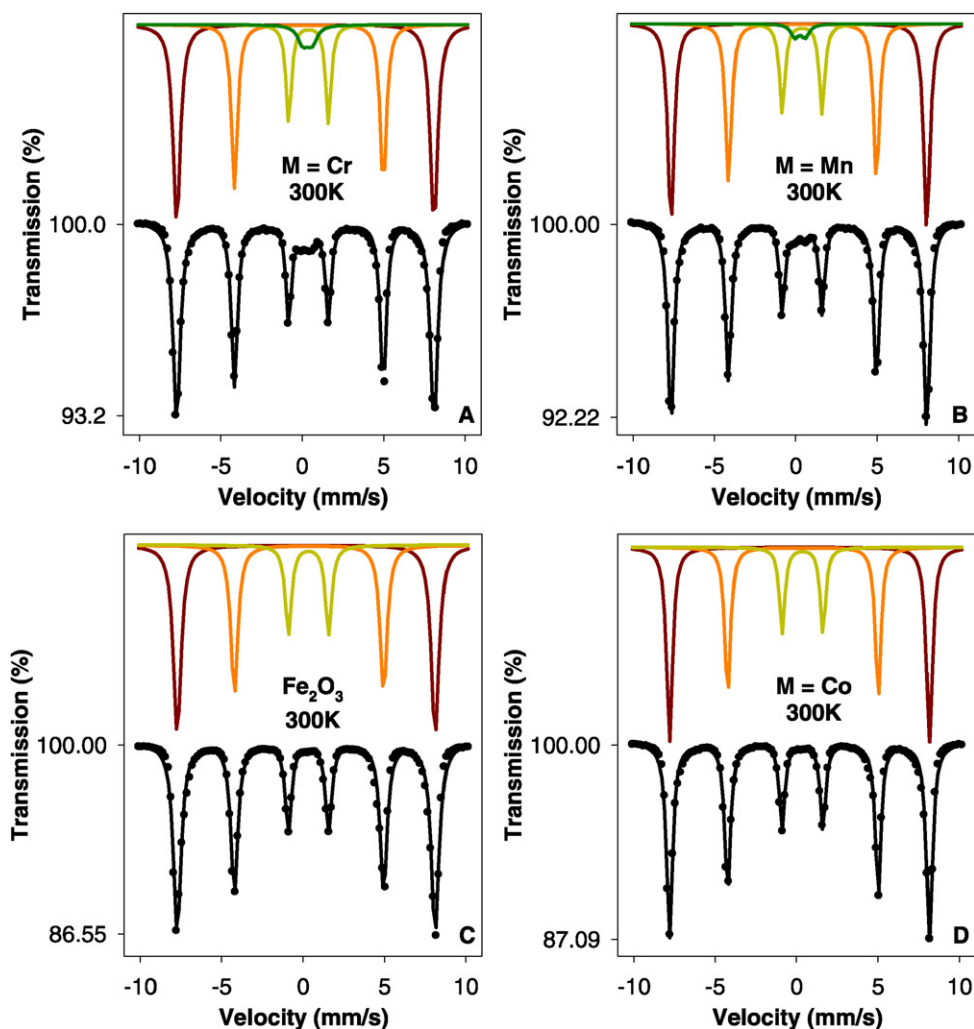


Fig. 5. (a) ^{57}Fe Mössbauer spectra of titled $\text{Fe}_{1.82}\text{M}_{0.18}\text{O}_3$ ($\text{M} = \text{Cr}, \text{Mn}, \text{and Co}$) catalysts.

between these sites ($\text{Fe}^{2+} \rightleftharpoons \text{Fe}^{3+}$). Mössbauer spectroscopy is an ideal probe for gaining insight into the structure/coordination and valence state [40]. We performed Mössbauer spectroscopy measurements to elucidate the nature of the Fe sites formed and their dynamics.

Hematite crystallizes in the Al_2O_3 (corundum) structure with a closely packed oxygen lattice, with Fe^{3+} cations occupying octahedral sites. It exhibits a complex magnetic behavior, being antiferromagnetic at low temperatures ($T < 80$ K) and undergoing a Morin transition at $T_M > 260$ K involving a spin flip, leading to a weak ferrimagnetic state, before becoming paramagnetic (Curie temperature) at high temperatures ($T_C \cong 955$ K). Its structure can be visualized as being composed of $\text{Fe}-\text{O}_3-\text{Fe}$ units (triplets) of closely packed oxygen atoms with Fe(III) on either side. The Fe(III) atoms in each of these $\text{Fe}-\text{O}_3-\text{Fe}$ units have opposite spins, being antiferromagnetically coupled as a result of superexchange interaction through the triad of oxygen atoms [41]. Mössbauer spectra of selected samples investigated in the present study are shown in Fig. 5, and the corresponding hyperfine structure parameters obtained by fitting the line shape are summarized in Table 3. For comparison, relevant hyperfine structure parameters obtained from

previous work [42,43] are also given in Table 3. Bulk crystalline hematite is characterized by an internal magnetic hyperfine field of 51.8 T at room temperature. Nanocrystalline hematite, on the other hand, has a smaller quadrupole splitting Δ and a room temperature magnetic hyperfine field of about 51 T. Deviations from ideal chemistry and crystallinity usually relate to particle size effects and/or substitution effects [42]. In the present investigation, Mössbauer spectra were recorded at room temperature for most of the samples. Enhanced contribution due to super-paramagnetic nanoparticles was observed in room temperature Mössbauer spectra of Fe/Ni , Fe/Zn , and Fe/Ce samples. Therefore, Mössbauer spectra of these samples also were recorded at liquid N_2 temperature (78 K). At 78 K, the recoil-free fraction increased, and the size of the effect increased. More significantly, as the sample is cooled, spin-lattice relaxation slowed, and a magnetic hyperfine structure developed, facilitating identification of various iron phases in the samples [41]. This finding is in agreement with the report of Janot et al. [44], who confirmed the variations in magnetic properties for natural hematites of small particle size. In general, samples containing particles smaller than 8 nm showed a super-paramagnetic doublet at room temperature. Interestingly,

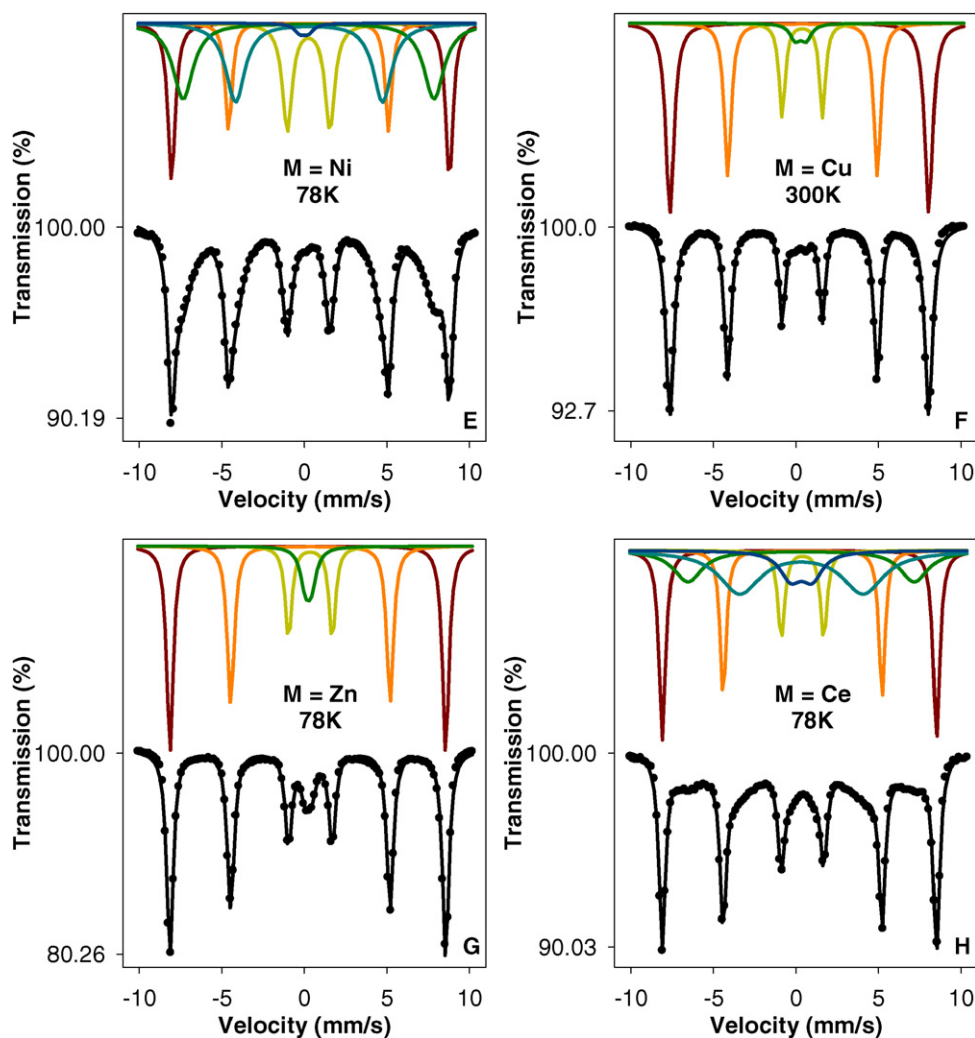


Fig. 5. (b) ^{57}Fe Mössbauer spectra of titled $\text{Fe}_{1.82}\text{M}_{0.18}\text{O}_3$ ($\text{M} = \text{Ni}, \text{Cu}, \text{Zn}, \text{and Ce}$) catalysts.

samples of Fe/Ni, Fe/Zn, and Fe/Ce ferrites were composed of 5 to 8 nm particles, as confirmed by TEM (presented below).

^{57}Fe Mössbauer spectra of pristine Fe_2O_3 sample (Fig. 5C) exhibits a six-line Zeeman spectrum at room temperature. The value of the isomer shift of Fe_2O_3 is typical of a trivalent iron (Table 3). Deviations in isomer shift (δ), quadrupole splitting (Δ), and magnetic hyperfine field (H_{int}) parameters between the present nanocrystalline $\alpha\text{-Fe}_2\text{O}_3$ and reported bulk $\alpha\text{-Fe}_2\text{O}_3$ could be simply a grain size effect. To further study the association between grain size and the hyperfine magnetic parameters, a sample of pristine $\alpha\text{-Fe}_2\text{O}_3$ was further calcined at 700°C for 12 h in flowing N_2 gas and analyzed by Mössbauer spectroscopy. On calcination of nanocrystalline $\alpha\text{-Fe}_2\text{O}_3$, the magnetic field strength (H) was found to increase from 50.1 to 51.6 T (Table 3); this increase appears to be related to particle size. Changes in isomer shift and quadrupole splitting parameters with increasing particle size were also seen (Table 3). These findings support the idea that particle size through local fields influences the hyperfine structure. Doping metal cations into hematite ($\alpha\text{-Fe}_2\text{O}_3$) modifies the magnetic hyperfine field and also influences other properties, such as reducibility and covalency of hematite particles. These effects appear to depend on

Table 3
Magnetic field (H), quadrupole splitting (Δ) and isomer shift (δ^a) measurements

Metal doped iron oxides	Cryst. size (nm) ^b	Temperature	H (T)	Δ (mm/s)	δ^a (mm/s)
$\text{Fe}_{2-x}\text{M}_x\text{O}_3$			± 0.2	± 0.01	± 0.01
$\text{Fe}_{1.82}\text{Cr}_{0.18}\text{O}_3$	12.5	300 K	50.0	-0.109	0.365
$\text{Fe}_{1.82}\text{Mn}_{0.18}\text{O}_3$	nd	300 K	49.7	-0.112	0.365
$\text{Fe}_{1.82}\text{Co}_{0.18}\text{O}_3$	16.3	300 K	50.4	-0.107	0.345
$\text{Fe}_{1.82}\text{Ni}_{0.18}\text{O}_3$	11.8	78 K	53.1	0.056	0.456
$\text{Fe}_{1.82}\text{Cu}_{0.18}\text{O}_3$	10.7	300 K	49.5	-0.095	0.374
$\text{Fe}_{1.82}\text{Zn}_{0.18}\text{O}_3$	10.1	78 K	52.7	-0.080	0.363
$\text{Fe}_{1.82}\text{Ce}_{0.18}\text{O}_3$	7.1	78 K	52.3	-0.095	0.377
Fe_2O_3^c	12.8	300 K	50.1	-0.087	0.354
$\text{Fe}_2\text{O}_3^{c,d}$	28	300 K	51.6	-0.077	0.387
Fe_2O_3^e	Bulk	295 K	51.75	-0.197	0.37
Fe_2O_3^f	Bulk	80 K	-	-0.22	-

^a Relative to $\alpha\text{-Fe}$.

^b Calculated from XRD using Scherrer equation.

^c Present study.

^d Calcined at 700°C for 12 h in N_2 flow.

^e Ref. [42].

^f Ref. [43].

the nature of the dopant metal cation. In general, the radii of substituent ions (M^{n+}) differ from those of Fe^{3+} . Such differences produce distortions in the crystal structure. A size mismatch between the Fe^{3+} and substituent (M^{n+}) cations leads to an electric field gradient (EFG) that measures the asphericity or distortion of the FeO_6 octahedra. Mössbauer spectra of our metal-doped iron oxide samples were analyzed as a superposition of a Zeeman sextet and a doublet. The former comes from the large grain-sized ferromagnetic particles, whereas the later feature is due to super-paramagnetic small particles. The physics underlying these observations can be summarized as follows.

Difference in line shape between samples with large and small particles come largely because the net magnetic field is finite in the former but vanishes in the later. In microcrystalline samples, the magneto-anisotropic energy may be of the same order of magnitude as the thermal energy (kT), where k represents the Boltzmann constant and T represents the absolute temperature. The magneto-anisotropic energy represents the energy required to rotate the magnetization direction and is found to be proportional to the particle volume (V) and magneto-crystalline anisotropy constant (K). In a simplistic form, the spin-lattice relaxation time, τ , can be written [45] as

$$\tau = \tau_0 \exp(KV/kT).$$

The spin-lattice relaxation time τ is short for small-sized ($V <$) particles, whereas the reverse is the case for large-sized ($V >$) particles. For an ^{57}Fe nucleus to see a magnetic field H_{int} , the nuclear magnetic moment must precess about the local magnetic field for at least one cycle, also called the Larmor precession time, τ_1 . In general, a super-paramagnetic doublet will be observed when $\tau < \tau_1$, a circumstance in which the magnetic field averages out to zero, because atomic spins (producing the field) fluctuate at a rate exceeding the time (τ_1) needed to sense that field. τ_1 may be visualized as the interaction time, that is, the time needed for a nucleus to sense the local field. At the other extreme, a well-resolved six-line magnetic hyperfine structure will be observed when $\tau > \tau_1$, that is, when fluctuations in magnetization are much slower than the Larmor precession time. In these Mossbauer effect experiments, the characteristic time, τ_1 , is on the order of 10^{-8} – 10^{-9} s, which fixes a threshold particle size of about 10 nm to observe a magnetic hyperfine structure at room temperature. Cooling a small grain-sized sample from room temperature to 78 K slows the spin-lattice relaxation time, leading to a six-line Zeeman spectrum [46].

Spatial variations in interaction fields can lead to broadening of lines. Generally, the incorporation of metal cations with charges other than 3^+ in $\alpha-Fe_2O_3$ will change the electrical neutrality of the crystal lattice, and countercharges will be required to restore electrical neutrality. In the case of formation of solid solutions of M^{n+} ($n \neq 3$) ions and $\alpha-Fe_2O_3$, this charge balance is most likely achieved by the creation/formation of oxygen vacancies. The variation in the quadrupole-splitting values observed in this study (Table 3) provides a direct measure of the distortion caused by oxygen vacancies. In conclusion,

the Mössbauer spectroscopy through hyperfine magnetic interaction parameters is a rather sensitive probe of the size, crystallite distortion, and substructure of metal-doped $\alpha-Fe_2O_3$ particles.

3.7. TEM

To study surface morphology and explore the structural features at the grain level, TEM studies were performed on various metal-doped iron oxide-based $Fe_{1.82}M_{0.18}O_3$ ($M = Cr, Mn, Co, Ni, Cu, Zn, \text{ and } Ce$) catalysts. The corresponding TEM images thus obtained are presented in Figs. 6A–6H. In general, the existence of grains with an associated size of 5–20 nm was observed (Table 1). To gain insight into their crystal structure, digital diffraction patterns (DDPs) acquired from the nanoparticles assemblies of each sample are presented as insets in the respective TEM images. The different rings and spots account for the existence of periodic contrasts in the original experimental micrographs, which correspond to different sets of atomic planes of the crystalline structure. The geometric arrangements of these reflections are directly related to the structural aspects of the analyzed crystals. Because of this, the DDPs are very useful in phase recognition [47]. Table 4 displays the measured lattice spacing based on the rings in the diffraction pattern and compares them with the known lattice spacing for bulk Fe_2O_3 along with their respective hkl indexes from the PDF database. The position and relative intensity of all of the diffraction rings closely match the standard Fe_2O_3 powder diffraction data. All of the catalysts prepared in this investigation exhibited nanosize grains. The high surface area-to-volume ratio in nanoparticles leads to modification in the surface structure and hence to enhanced surface features. Nanocrystalline particles are known to be more reactive than larger particles due to the higher relative concentration of crystallographic areas where atoms exist with low coordination numbers. On the whole, all of the samples investigated exhibited uniform particle size distribution; however, a significant number of crystals displayed a pattern of parallel high-contrast light and dark bands extending across their surfaces. As reported previously, it may be a diffraction phenomenon caused by the presence of a surface layer of different phase or crystallographic orientation from that of the crystal underneath [47]. Substitution of iron by larger substituent metal ions in the hematitic crystal lattice generates considerable stress in the system. To overcome this stress, the equilibrium particle size is shifted toward smaller particles, because the ratio of strain to surface effects becomes greater for larger particles.

3.8. Structure–WGS activity correlated

Our findings demonstrate that simultaneous precipitation of substituent metal cation (M^{n+}) with Fe^{3+} leads to the formation of hematite-like $Fe_{1.82}M_{0.18}O_3$ phase, which on activation transforms into either an inverse or mixed $Fe_{2.73}M_{0.27}O_4$ spinel. The overall WGS activity depends on various parameters, including operation conditions, the nature of the substituent ion incorporated, and the covalency of the $Fe^{III} \leftrightarrow Fe^{II}$ redox couple in the resultant catalyst. Topsøe and Boudart [48]

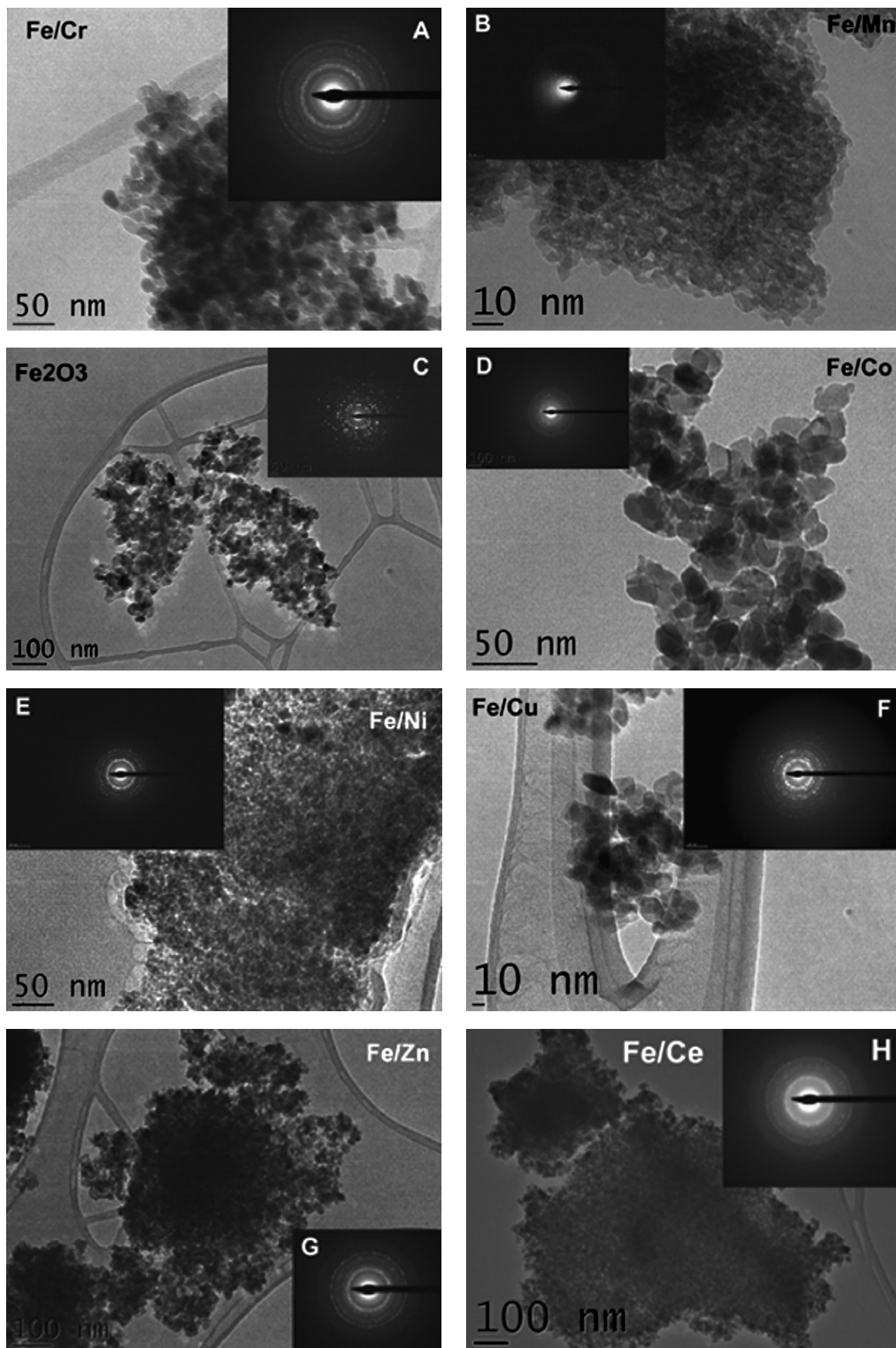


Fig. 6. TEM images of various $\text{Fe}_{1.82}\text{M}_{0.18}\text{O}_3$ (M = Cr, Mn, Co, Ni, Cu, Zn, and Ce) catalysts. The insets in the respective images are digital diffraction patterns (DDPs) obtained from the corresponding nanoparticles assemblies.

Table 4

Measured lattice spacing, d (Å), based on the rings in the insets of Figs. 6A–6H and standard atomic spacing for Fe_2O_3 along with their respective hkl indexes from the PDF database

Sample	Ring/ d (Å)							
	1	2	3	4	5	6	7	8
$\text{Fe}_{1.82}\text{Cr}_{0.18}\text{O}_3$	3.641	2.731	2.457	2.184	1.787	1.638	–	1.404
$\text{Fe}_{1.82}\text{Mn}_{0.18}\text{O}_3$	–	–	–	–	–	–	–	–
Fe_2O_3	3.932	2.73	2.34	–	1.966	–	–	–
$\text{Fe}_{1.82}\text{Co}_{0.18}\text{O}_3$	3.389	2.808	2.521	2.184	1.966	1.666	–	–
$\text{Fe}_{1.82}\text{Ni}_{0.18}\text{O}_3$	3.932	2.89	2.397	2.04	1.854	1.585	–	–
$\text{Fe}_{1.82}\text{Cu}_{0.18}\text{O}_3$	–	2.808	–	2.286	1.787	1.638	–	1.404
$\text{Fe}_{1.82}\text{Zn}_{0.18}\text{O}_3$	3.933	2.731	2.397	2.048	1.855	1.611	–	–
$\text{Fe}_{1.82}\text{Ce}_{0.18}\text{O}_3$	–	2.731	–	–	1.724	–	–	1.445
Fe_2O_3^a	3.684	2.7	2.519	2.2070	1.8406	1.6941	1.4859	1.4538
hkl^a	012	104	110	113	024	116	214	300
Int- f^a	30	100	70	20	40	45	30	30

^a PDF-ICDD: 033-0664.

found that expansion of tetrahedral sites and contraction of octahedral sites leads to increased covalency in the system and improved electron-hopping capabilities between $\text{Fe}^{\text{III}} \leftrightarrow \text{Fe}^{\text{II}}$ octahedral sites. Moreover, improving the covalency of the catalysts improves the WGS activity [39]. Boreskov has demonstrated that the octahedral Fe^{2+} and Fe^{3+} ions located in the magnetite-based structure function as a redox couple, and that magnetite-based catalysts can be highly effective for the complete dissociation of water into hydrogen and adsorbed oxygen under reaction conditions. Water dissociation causes the oxidation of Fe^{2+} centers to Fe^{3+} and liberates hydrogen. The oxidized iron centers may subsequently be reduced by CO, thereby producing CO_2 to complete the reaction loop [39]. Cr_2O_3 is a well-known refractory oxide. The presence of chromium restricts the rapid thermal sintering of Fe_3O_4 , thereby enhancing the WGS activity of the Fe/Cr catalyst. It is proposed that iron-chromia forms an inverse spinel structure and that Cr^{3+} replaces equal amounts of Fe^{2+} and Fe^{3+} from the octahedral sites, with the displaced Fe^{2+} consequently located in tetrahedral sites [49]. In the case of our Fe/Mn catalysts, formation of FT product (methane) was observed at the expense of the H_2 produced by the WGS reaction. The addition of Cu to iron oxide resulted in improved reducibility of Fe^{3+} into Fe^{2+} species, as evidenced by the TPR results, thereby promoting WGS activity. On doping with Cu, the mobility of lattice oxygen and hydroxyl groups increased, due to the greater electronegativity of Cu (1.9) relative to Fe (1.8), thereby improving catalytic activity [50]. Iron–ceria-based WGS catalysts are promising, because the oxygen storage capacity (OSC) of ceria and the cooperative effect of Ce–Fe leads to active sites. Interestingly, both iron and ceria undergo facile charge-transfer reactions between $\text{Fe}^{\text{III}} \leftrightarrow \text{Fe}^{\text{II}}$ and $\text{Ce}^{\text{IV}} \leftrightarrow \text{Ce}^{\text{III}}$ redox couples, respectively; the synergism between the two couples could be responsible for the improved WGS activity. In addition, the increased WGS activity with increase in temperature could be due to the improved OSC of ceria [51]. A noticeable interaction between iron and other substituent metal was interpreted in terms of the changes in the lattice parameters and isomer

shifts, δ . The synergistic effect can be attributed primarily to the formation of either inverse or mixed spinels of composition $\text{A}_{(1-\delta)}\text{B}_\delta[\text{A}_\delta\text{B}_{(2-\delta)}]\text{O}_4$, which have a highly facile $\text{Fe}^{3+} \leftrightarrow \text{Fe}^{2+}$ redox couple. The resultant WGS activity can be related to the degree of covalency ($\text{Fe}^{3+} \leftrightarrow \text{Fe}^{2+}$ redox couple), which in turn depends on the operation conditions and catalyst formulation.

4. Conclusion

Simultaneous precipitation of Fe(III) nitrates along with substituent metal nitrates (of Cr, Mn, Co, Ni, Cu, Zn, or Ce) results in the formation of high-surface area nanocrystalline catalysts. XRD data analyses of activated catalysts have established the existence of $\text{Fe}_{2.73}\text{M}_{0.27}\text{O}_4$ ($\text{M} = \text{Cr, Mn, Co, Ni, Cu, Zn, and Ce}$)-type spinels. The synergistic effect between iron and the other metal substituent leads to the formation of either inverse or mixed spinel of composition $\text{A}_{(1-\delta)}\text{B}_\delta[\text{A}_\delta\text{B}_{(2-\delta)}]\text{O}_4$. Incorporation of metal cations into the hematite ($\alpha\text{-Fe}_2\text{O}_3$) crystal structure modifies the magnetic field and also influences the reducibility of hematite particles, as was observed in Mössbauer spectroscopy and TPR studies, respectively. Mössbauer spectroscopy through hyperfine magnetic interaction parameters is a rather sensitive probe of the size, crystallite distortion, and substructure of metal-doped $\alpha\text{-Fe}_2\text{O}_3$ particles. Based on the present findings, it can be concluded that Fe/Ce-modified ferrite is a promising system for the WGS reaction during steam-rich operations. The conditions of operation play a vital role on the eventual WGS activity exhibited by each individual catalyst investigated in this study.

Acknowledgments

Financial support was provided by the U.S. Department of Energy (grant DE-PS36-03GO93007) and the National Science Foundation (grant DMR 04-56472).

Supplementary material

The online version of this article contains additional supplementary material.

Please visit DOI:10.1016/j.jcat.2007.10.018.

References

- [1] E. Kikuchi, S. Uemiya, N. Sato, H. Inoue, T. Matsuda, *Chem. Lett.* 489 (1989) 1.
- [2] S. Uemiya, N. Sato, H. Ando, E. Kikuchi, *Ind. Eng. Chem. Res.* 30 (1991) 585.
- [3] A. Basile, E. Drioli, F. Santella, V. Violante, G. Capannelli, G. Vitulli, *Gas Sep. Purif.* 10 (1996) 53.
- [4] A. Basile, A. Criscuoli, F. Santella, E. Drioli, *Gas Sep. Purif.* 10 (1996) 243.
- [5] A. Criscuoli, A. Basile, E. Drioli, O. Loiacono, *J. Membr. Sci.* 181 (2001) 21.
- [6] A. Criscuoli, A. Basile, E. Drioli, *Catal. Today* 56 (2000) 53.
- [7] Y.S. Lin, *Sep. Purif. Technol.* 25 (2001) 39.
- [8] S.G. Deng, Y.S. Lin, *Ind. Eng. Chem. Res.* 34 (1995) 4063.
- [9] Y.S. Lin, I. Kumakiri, B.N. Nair, H. Alsyouri, *Sep. Purif. Methods* 32 (2002) 229.
- [10] J. Dong, W. Liu, Y.S. Lin, *AIChE J.* 46 (2000) 1957.
- [11] R.C.C. Costa, F. Lelis, L.C.A. Oliveira, J.D. Fabris, J.D. Ardisson, R.R.A. Rios, C.N. Silva, R.M. Lago, *Catal. Commun.* 4 (2003) 525.
- [12] M.S. Selim, G. Turkey, M.A. Shouman, G.A. El-Shobaky, *Solid State Ionics Diffusion React.* 120 (1999) 173.
- [13] C.G. Ramankutty, S. Sugunan, B. Thomas, *J. Mol. Catal.* 187 (2002) 105.
- [14] L.C.A. Oliveira, R.V.A. Rios, W.N. Mussel, J.D. Fabris, R.M. Lago, *Stud. Surf. Sci. Catal.* 130 (2000) 2165.
- [15] G.C. Araujo, M.C. Rangel, *Catal. Today* 62 (2000) 201.
- [16] B.M. Reddy, A. Khan, *Catal. Surv. Asia* 9 (2005) 155.
- [17] H.P. Klug, L.E. Alexander, *X-Ray Diffraction Procedures for Polycrystalline and Amorphous Materials*, second ed., Wiley, New York, 1974.
- [18] R.D. Shannon, *Acta Crystallogr. A* 32 (1976) 751; A. Navrotsky, O.J. Kleppa, *J. Inorg. Nucl. Chem.* 29 (1967) 2701.
- [19] A.D. Krawitz, *Introduction to Diffraction in Materials Science and Engineering*, Wiley-Interscience, New York, 2001.
- [20] C. Rhodes, G.J. Hutchings, A.M. Ward, *Catal. Today* 23 (1995) 43.
- [21] C. Rhodes, B.P. Williams, F. King, G.J. Hutchings, *Catal. Commun.* 3 (2002) 381.
- [22] E. Xue, M. O’Keeffe, J.R.H. Ross, *Catal. Today* 30 (1996) 107.
- [23] J.A. Dumesic, H. Tøpsoe, *Adv. Catal.* 26 (1977) 121.
- [24] M.V. Twigg, *Catalyst Handbook*, second ed., Wolfe Publishing, London, 1989, pp. 268–288.
- [25] D.S. Newsome, *Catal. Rev.-Sci. Eng.* 21 (1980) 275.
- [26] E.F. Armstrong, T.P. Hilditch, *Proc. R. Soc. A* 97 (1920) 265.
- [27] J.O. Edstrom, *J. Iron Steel Inst.* 175 (1953) 289.
- [28] M.V.C. Sastri, R.P. Vishwanath, B. Vishwanath, *Int. J. Hydrogen Energy* 7 (1982) 951.
- [29] P.A. Webb, MIC Technical Publications, January 2003, pp. 1–12.
- [30] J.C. Gonzalez, M.G. Gonzalez, M.A. Laborde, N. Moreno, *Appl. Catal.* 20 (1986) 3.
- [31] O.J. Wimmers, P. Arnoldy, J.A. Moulijn, *J. Phys. Chem.* 90 (1986) 1331.
- [32] E.P. Reddy, B. Sun, P.G. Panagiotis, *J. Phys. Chem. B* 108 (2004) 17198.
- [33] R. Brown, M.E. Cooper, D.A. Whan, *Appl. Catal.* 3 (1982) 177.
- [34] A. Khan, P.G. Smirniotis, *J. Mol. Catal. A Chem.* (2007), in press.
- [35] J.Y. Kim, J.A. Rodriguez, J.C. Hanson, A.I. Frenkel, P.L. Lee, *J. Am. Chem. Soc.* 123 (2003) 10684.
- [36] G.C. de Araujo, M. do C. Rangel, *Catal. Today* 62 (2000) 201.
- [37] F. Giordano, A. Trovarelli, C. de Leitenburg, M. Giona, *J. Catal.* 193 (2000) 273.
- [38] D.G. Reithwisch, J.A. Dumesic, *Appl. Catal.* 97 (1986) 109.
- [39] G.K. Boreskov, *Kinet. Katal.* 11 (1970) 374.
- [40] S. Morup, J.A. Dumesic, H. Topsoe, in: R.L. Cohen (Ed.), *Applications of Mössbauer Spectroscopy*, vol. II, Academic Press, New York, 1980, p. 1.
- [41] N.N. Greenwood, T.C. Gibb, *Mössbauer Spectroscopy*, Chapman & Hall, London, 1971.
- [42] E. Murad, *J. Phys. E* 17 (1984) 736.
- [43] J. Gastebois, J. Quidort, *Compt. Rend.* 253 (1961) 1257.
- [44] C. Janot, H. Gibert, C. Tobias, *Bull. Soc. Fr. Miner. Cristallogr.* 96 (1973) 281.
- [45] L. Neel, *Ann. Geophys.* 5 (1949) 99.
- [46] S. Morup, in: G.J. Long (Ed.), *Applications of Mössbauer Spectroscopy Applied to Inorganic Chemistry*, vol. 2, Plenum, New York, 1988.
- [47] C. Lopez-Cartes, J.A. Perez-Omil, J.M. Pintado, J.J. Calvino, Z.C. Kang, L. Eyring, *Ultramicroscopy* 80 (1999) 19.
- [48] H. Topsoe, M. Boudart, *J. Catal.* 31 (1973) 346.
- [49] H. Topsoe, J.A. Dumesic, M. Boudart, *J. Catal.* 28 (1973) 477.
- [50] W.F. Podolski, Y.G. Kim, *Ind. Eng. Chem. Process. Des. Dev.* 13 (1974) 415.
- [51] F.J. P-Alonso, I. M-Cabrera, M.L. Granados, F. Kapteijn, J.L.G. Fierro, *J. Catal.* 239 (2006) 340.